Research Article

Hang Wang, Aiqin Wang*, Changyi Li, Xingsheng Yu*, Jingpei Xie, Tingting Liang, and Chenlu Liu

# Effects of rare earth metals on microstructure, mechanical properties, and pitting corrosion of 27% Cr hyper duplex stainless steel

https://doi.org/10.1515/rams-2022-0284
received August 18, 2022; accepted October 25, 2022

**Abstract:** This research focuses on the addition of low-cost rare earth metals (REMs) to improve the comprehensive properties of hyper duplex stainless steels (DSSs). The effects of REM on the microstructure, mechanical properties, and pitting corrosion of hyper DSSs were analyzed by optical/scanning electron microscope metallographic examination, X-ray diffraction analysis, tensile test, impact test, and potentiodynamic polarization test. With the addition of REM, micro/nanoscale REM inclusions were formed, and the microstructure of the alloy was refined. With the increasing content of REM, the average diameter and area of inclusions in the alloy decreased at first and then increased. While the mechanical properties showed a trend of first increasing and then decreasing. An appropriate amount of stable REM inclusions could reduce the susceptibility of pitting corrosion and improve the pitting corrosion resistance of the alloy. The hyper DSSs with REM content in the range of 0.018–0.031 wt% have excellent mechanical properties and pitting resistance.

**Keywords:** hyper duplex stainless steel, rare earth metals, microstructure, mechanical properties, pitting corrosion

*** Corresponding author: Aiqin Wang,** School of Materials Science and Engineering, Henan University of Science and Technology, Luoyang 471023, People's Republic of China, e-mail: aiqin_wang888@163.com
*** Corresponding author: Xingsheng Yu,** Luoyang CITIC HIC Casting & Forging Co., Ltd, Luoyang 471039, People's Republic of China; CITIC Heavy Industries Co., Ltd, Luoyang 471039, People's Republic of China, e-mail: yuxingsheng2016@126.com
**Hang Wang:** School of Materials Science and Engineering, Henan University of Science and Technology, Luoyang 471023, People's Republic of China; Luoyang CITIC HIC Casting & Forging Co., Ltd, Luoyang 471039, People's Republic of China; CITIC Heavy Industries Co., Ltd, Luoyang 471039, People's Republic of China
**Changyi Li:** Luoyang CITIC HIC Casting & Forging Co., Ltd, Luoyang 471039, People's Republic of China; CITIC Heavy Industries Co., Ltd, Luoyang 471039, People's Republic of China
**Jingpei Xie, Tingting Liang, Chenlu Liu:** School of Materials Science and Engineering, Henan University of Science and Technology, Luoyang 471023, People's Republic of China

## 1 Introduction

Duplex stainless steel (DSS) composed of ferrite and austenite has shown excellent mechanical properties and corrosion resistance, which is widely used in the oil and gas industry, seawater environment, desalination, and chemical fertilizer industry [1–3]. In recent years, to meet the needs of extremely harsh working conditions, such as deep-sea oilfield exploitation and flue gas desulfurization, highly alloyed hyper DSSs with pitting resistance equivalent number (PREN) values (wt% Cr + 3.3 [wt% Mo + 0.5 wt% W] + 30 wt% N) greater than 50, such as SAF2707HD and SAF3207HD, have received more and more attention. The hyper DSSs with excellent mechanical properties and corrosion resistance usually have high contents of Cr, Ni, and Mo, which is more likely to form harmful secondary phases, such as χ phase in ternary Fe–Cr–Mo system and quaternary Fe–Cr–Ni–Mo system [4–6]. Usually, the brittle intermetallic compounds represented by σ phase and χ phase are easily precipitated in the casting cooling process, hot rolling slow cooling process, and welding thermal cycles. Thus, the Cr and Mo element-depleted zones around the brittle intermetallic compounds can be formed, which reduces the mechanical properties and corrosion resistance of DSSs. The secondary phases can be eliminated by appropriate solid solution heat treatment [7,8]. Kim et al. [9] reported that the addition of Ce with a content of 50–100 ppm can effectively delay the precipitation of σ and χ phases in 27Cr–7Ni–2.5Mo–3.3W –0.35N hyper DSSs during isothermal annealing at temperature range of 873–1,273 K for 1–1,000 min, thereby inhibiting the degradation of mechanical properties.

However, excessive Ce (450 ppm) formed Ce-rich particles, which result in a low concentration of Ce in the matrix, leading to the degradation of mechanical properties. Jeon et al. [10] indicated that the addition of Ce (0.056 wt%) can reduce the precipitation of σ phase in 2707HD hyper DSSs during isothermally aged at 850°C for 10 and 30 min, thereby retarding the decrease in intergranular corrosion resistance of the alloy. Extensive research works have been carried out to inhibit the phase of intermetallic compounds and control the formation of nonmetallic inclusions, so as to improve the quality of DSSs. In addition, in order to improve the weldability of DSSs, Świerczyńska et al. [11] studied the hydrogenation of DSSs welded joints prone to hydrogen embrittlement under cathodic protection in artificial seawater environment and established mathematical models to analyze the mechanical properties of welded joints under cathodic protection conditions. Varbai et al. [12] developed the Johnson–Mehl–Avrami–Kolmogorov equations parameters to accurately predict the austenite/ferrite ratios in the heat-affected zone.

Hyper DSSs are usually used in harsh working conditions with high content of chloride. It is valuable in industrial applications to optimize the composition of alloy through the addition of some beneficial elements such as low-cost rare earth metals (REM) to improve its comprehensive properties. The standard free energy of $(REM)_xS_y$ and $(REM)_2O_3$ is lower than that of non-metallic inclusions in alloys, such as $Al_2O_3$ and MnS, which is easily served as the starting point of pitting corrosion in a chloride-exposure environment [13–16]. The addition of an appropriate amount of REM tends to form spherical REM inclusions, which can improve its pitting resistance [17,18]. In addition, unlike angular MnS-type inclusions, spherical REM inclusions are less likely to form concentration gradient at grain boundaries, improving the toughness of the alloy [19]. NithinRaj et al. [20,21] reported that ASTM A890 7A hyper DSSs with 0.0109 wt% REM addition has a stable oxide layer and high PREN equivalent. Coupled with its higher hardness, 7A hyper DSSs were more suitable for severe erosion–corrosion and high-speed sliding wear environments than grade 5A and 6A super DSSs. Ma et al. [22] indicated that the addition of REM (0.056 wt%) improved the hot workability of 23Cr–5Ni–3.2Mo–0.17N DSSs. The micro-alloying of REM can reduce the mismatch of hardness between ferrite and austenite, improve the development of dynamic recrystallization, and narrow the flow instability zone in the region of heat deformation parameters. Ha et al. [23] demonstrated that the size and surface density of REM inclusions formed by adding 0.067 wt% REM to 25% Cr super DSSs decreased, thus improving the pitting corrosion resistance of the alloy. Liu et al. [24] found that the purification and micro-alloying effects of REM significantly can improve the impact energy and ultimate tensile strength and inhibit the growth of fatigue cracks of 718H pre-hardened mold steel. However, the excessive addition of REM up to 0.07 wt% deteriorated the mechanical properties. That is to say, the increase of REM content within a certain range consistently improved high-carbon chromium-bearing steel transverse and longitudinal impact toughness [25]. However, the excessive addition of REM severely deteriorated the impact toughness. Yang et al. [26] presented that the addition of 0.0065 wt% REM can refine and modify the inclusions in high-carbon chromium-bearing steel, which exhibits shorter crack initiation life and longer crack propagation life. Therefore, compared to the steel without REM addition, the fatigue life was increased by more than 10 times in the very high-cycle fatigue regime. Jiang et al. [27] showed that the best combination of strength, upper shelf energy, and ductile to brittle transition temperature were obtained by adding 0.012 wt% REM into low alloy Cr–Mo–V steels. However, the excessive addition of REM led to the increase of large-size inclusions, which significantly deteriorates the impact toughness.

The hyper DSSs used under harsh corrosion conditions require not only excellent corrosion resistance but also strong mechanical properties. However, most of the related studies only focused on the effect of single REM content on super DSSs, in which more attention is paid to a single aspect of microstructure, mechanical properties, or corrosion resistance. Experimental alloys prepared by melting in our study have a high degree of purity, thus avoiding that large amounts of REM was added for deoxidation and desulfurization to be consumed. The addition of REM can form a certain percentage of REM inclusions with micro/nanoscale, which may have significant effects on microstructure, strength, impact toughness, and corrosion resistance. Till now, the mechanism of REM on the microstructure, mechanical properties, and corrosion resistance of hyper DSSs with higher strength and corrosion resistance equivalents is not studied systematically enough. The REM content that reveals the best mechanical properties and corrosion resistance has not yet been elucidated.

This work examined the 27% Cr hyper DSSs alloy containing REM. The effects of micro/nanoscale inclusions formed by the addition of REM in high-purity hyper DSSs on microstructure, mechanical properties, and pitting resistance were studied in detail. These results are helpful to understand the action mechanism of REM in hyper DSSs and provide theoretical guidance for the design and industrial application of hyper DSSs.

# 2 Experimental procedures

## 2.1 Material

High-purity metals, including Fe, Cr, Ni, Mo, Cu, Co, and ferrochromium nitride, were used as raw materials. The experimental alloy was melted in a vacuum induction furnace (ZG-100 type; Suzhou Zhenwu Electric Furnace Co., Ltd, Suzhou, China). Different contents of REM (65 ± 5 wt% Ce–35 ± 5 wt% La–0.05 wt% Nd–0.05 wt% Pr) with purity greater than 99% were added in the tapping stage. Table 1 shows the chemical composition of the test alloy. The samples (20 mm × 20 mm × 120 mm) were cut from the alloy by wire electrical discharge and solution treated at 1,100°C for 120 min followed by quenching in water.

## 2.2 Experimental methods

In order to observe the optical microstructure, the alloy was ground into 1,200 particles with SiC sandpaper, polished with emery gypsum, and etched with a solution composed of 2 g of potassium sulfite, 30 mL of hydrochloric acid, and 100 mL of water for 2–5 min. The fracture morphology and corrosion pit morphology were analyzed by scanning electron microscope (SEM; ZEISS EVO-18, Carl Zeiss AG, Jena, Germany), and the chemical composition of the inclusion was analyzed by energy dispersive spectrometer (EDS) attached to SEM.

Tensile properties and Charpy impact were tested according to ASTM A370 standard test methods. Cylindrical specimens with 6.25 mm in diameter and 25 mm in gage lengths were used to test the tensile properties by 2 mm·min$^{-1}$ on the testing machines (DDL300; Sinotest Equipment Co., Ltd, Changchun, China). The V-notched specimens (55 mm × 10 mm × 10 mm) were used to measure the Charpy impact on the testing machine (NI150C; NSC Testing Technology Co., Ltd, Beijing, China). Mechanical properties were determined by means of the average values of four specimens of each alloy. The data were reported as mean ± standard deviation values.

In order to study the effect of REM on the pitting resistance of the alloys, the action potential anodic polarization curve and electrochemical impedance were measured by an electrochemical workstation (Autolab PGSTAT128N; MetrohmAG, Herisau, Switzerland) in a deaerated 3.5 wt% NaCl solution at room temperature. The electrochemical experiment adopts a three-electrode system; the auxiliary electrode is a large-area graphite electrode; the reference electrode is a saturated calomel electrode; and the working electrode is a test alloy sample with an exposed area of 1 cm$^2$. The scan rate of the potentiodynamic polarization curve was 20 mV·min$^{-1}$, and the scan range was −600 to 1,200 mV.

# 3 Results and discussion

## 3.1 Effect of REM addition on microstructures

Figure 1 shows the optical metallographic structures of the test alloys. The alloys are solidified in the form of ferrite–austenite [28–30]. At first, the primary ferrite dendrite begins to be solidified, and the austenite phase is formed with the segregation of Ni and N elements into the melt. In the as-cast microstructure, the lighter phase is austenite, and the darker phases are ferrite and secondary phases. The secondary phases are dominated by the σ phase (Figure 2) from the ferrite phase after the slow cooling process in the ingot mold. It is obvious that the microstructure of DSS 1 alloy without the addition of REM is coarse dendrite, while with the addition of REM, the as-cast structure of the alloys is obviously refined, and the microstructure distribution is more uniform. When the content of REM increases to 0.057 wt%, the as-cast structure did not continue to be more significantly refined. After solution treatment at 1,100°C, the microstructure of

**Table 1:** Chemical compositions of the experimental alloys (wt%)

| Alloy designation | C | Si | Mn | Cr | Ni | Mo | Cu | Co | S | N | REM | Fe | PREN[1] |
|---|---|---|---|---|---|---|---|---|---|---|---|---|---|
| DSS 1 | 0.021 | 0.44 | 1.15 | 26.9 | 6.44 | 4.58 | 0.88 | 1.02 | 0.005 | 0.43 | 0 | Bal. | 54.9 |
| DSS 2 | 0.018 | 0.41 | 1.08 | 27.2 | 6.55 | 4.55 | 0.93 | 0.98 | 0.004 | 0.43 | 0.018 | Bal. | 55.1 |
| DSS 3 | 0.022 | 0.39 | 1.12 | 27.1 | 6.41 | 4.62 | 0.87 | 0.93 | 0.002 | 0.42 | 0.031 | Bal. | 55.0 |
| DSS 4 | 0.020 | 0.43 | 1.03 | 27.3 | 6.53 | 4.45 | 0.99 | 1.04 | 0.002 | 0.44 | 0.057 | Bal. | 55.2 |

[1]PREN = wt% Cr + 3.3(wt% Mo + 0.5 wt% W) + 30 wt% N.

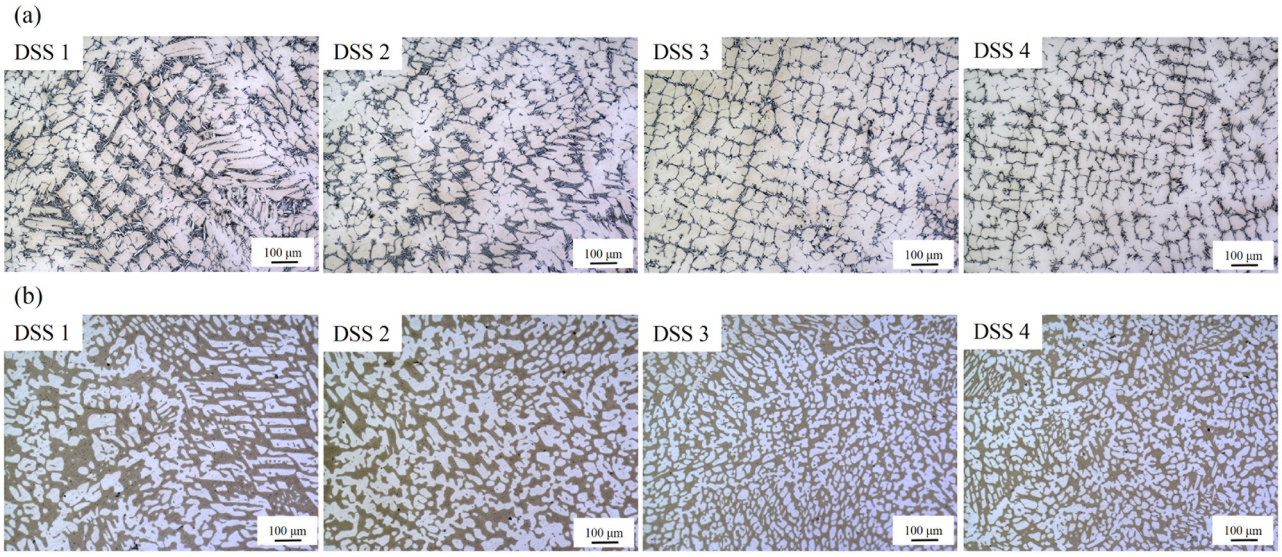


**Figure 1:** Microstructural evolution of (a) as-cast and (b) solution-treated alloys.

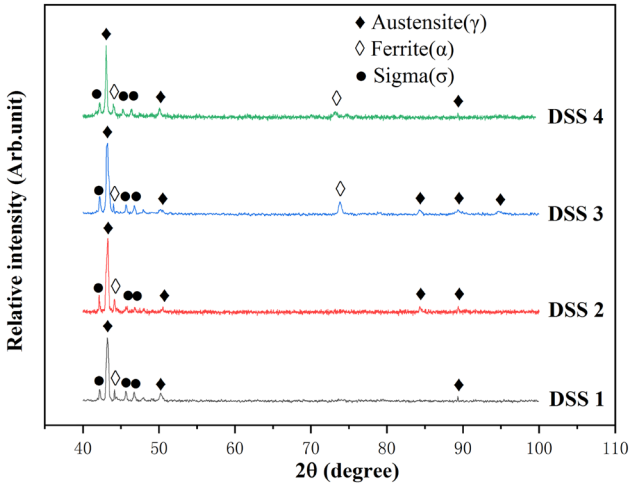


**Figure 2:** X-ray diffraction patterns of the as-cast alloys.

the alloy is a typical two-phase structure, that is, the lighter austenite phase is distributed on the darker ferrite matrix. It is basically consistent with the as-cast microstructure. Moreover, with the addition of REM, the size of austenite and ferrite became finer and more uniform.

The solidification of molten steel in non-equilibrium state usually forms grains by non-uniform nucleation. According to the heterogeneous nucleation theory put forward by Tumbull–Vonnegut [31], the interface of liquid metal needs to be provided by solid particles with a melting point higher than the liquid melting point in the solidification process. In addition, these high melting point particles need to have a low degree of mismatch with the metal crystal phase. Combining with oxygen and sulfur elements in steel, the REM of cerium and lanthanum with high chemical activity are easily formed into high-melting-point rare earth oxides, rare earth sulfides, and rare earth oxysulfides. It is generally believed that when the mismatch degree is less than 12%, the high melting point compound can become the core of non-spontaneous nucleation [32]. Gao et al. [33] reported that $Ce_2O_2S$ (0001) has a mismatch of 7.9% with the δ-Fe crystal plane (111), which is more likely to become the core of non-spontaneous nucleation. In addition, REM inclusions as secondary phase particles pinning grain boundaries and phase boundaries, leading to the inhibition of grain growth. Therefore, with the increase of REM content, the number of micro/nanoscale REM inclusions with high melting point increases, resulting in more core of non-spontaneous nucleation. At the same time, the more the REM atoms segregated at the grain boundary, the greater the drag effect on the grain boundary, resulting in the refinement of the as-cast structure of the alloy. Under the same heat treatment condition, the coarsening trend of the microstructure is basically the same, and the grain size after solution treatment was basically the same as that of the as-cast state.

## 3.2 Effect of the REM addition on the distribution of inclusions

Figure 3 shows the optical metallographic images of the as-cast alloys. Twenty fields were selected for each

sample to make statistics on the size and distribution of inclusions, as shown in Figure 4. The alloy with higher purity was obtained by experimental smelting, in which the content of oxygen (<50 ppm) and sulfur (<0.005 wt%) were lower, and the inclusion with a size <3 μm accounted for a large proportion of the alloy. The largest size of the inclusion was <10 μm. In general, when the content of REM increased to 0.031 wt% (DSS 3), the average diameter and area fraction of inclusions in DSS 1 alloy decreased gradually from 3.73 μm and 0.275% to 2.33 μm and 0.154%, respectively. At the same time, the proportion of inclusions <3 μm increases, while the proportion of inclusions >3 μm decreases greatly. However, when the REM addition increase to 0.057 wt% (DSS 4), the size and area of inclusions in the alloy increase sharply, in which the proportion of inclusions <3 μm decreases. However, the number of inclusions >3 μm

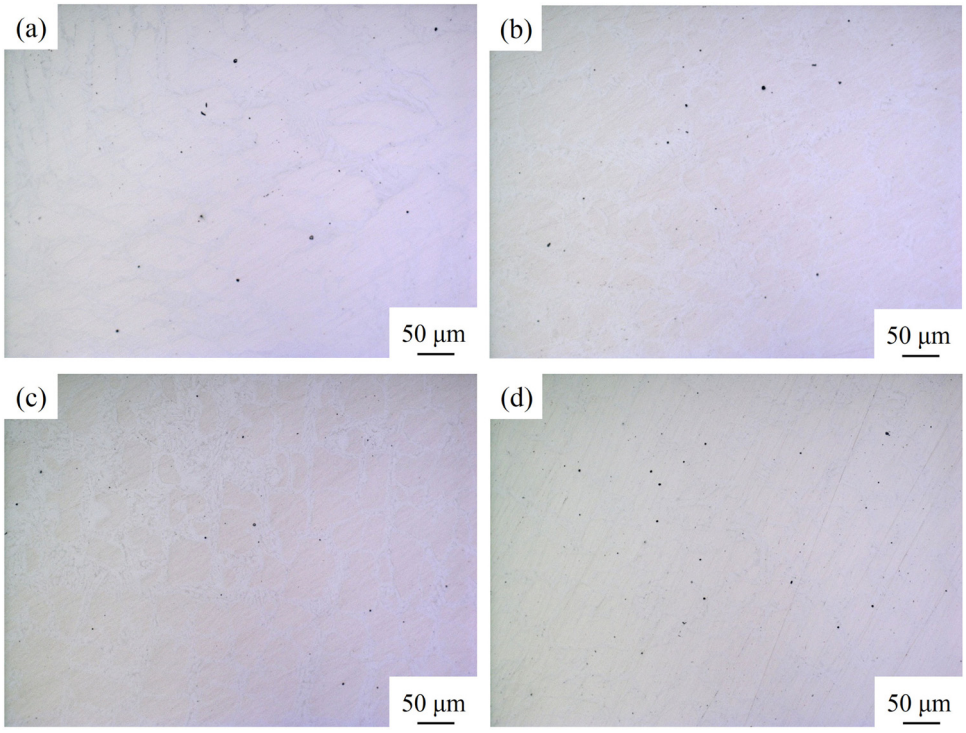


**Figure 3:** Distribution of inclusions in optical metallographic of the as-cast alloys: (a) DSS 1, (b) DSS 2, (c) DSS 3, and (d) DSS 4.

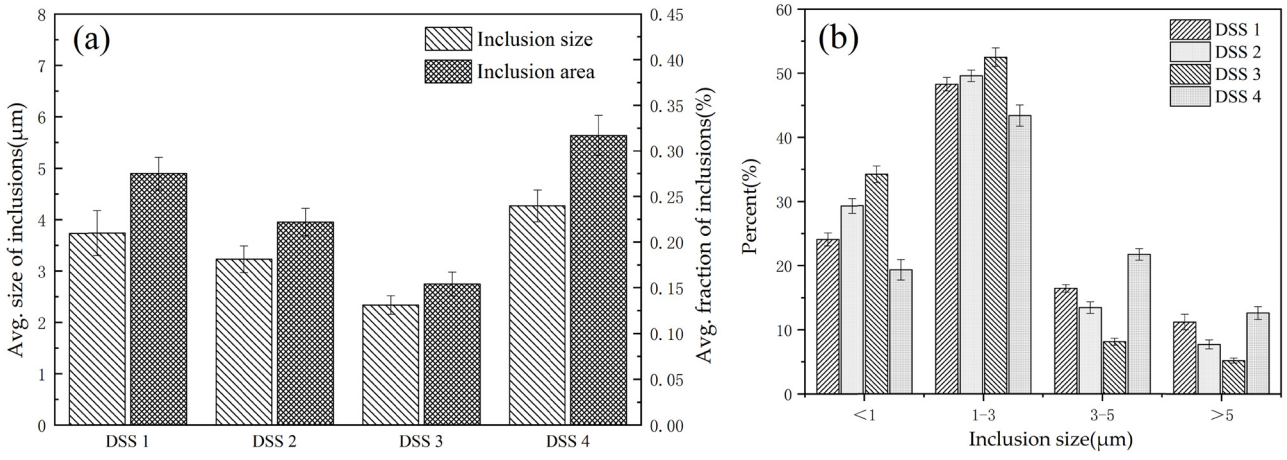


**Figure 4:** Effects of REM addition on the size, area, and distribution of inclusions per frame area of the alloys: (a) the average size and fraction of inclusions and (b) size distribution of inclusions.

increases obviously. Therefore, the optimum content range of REM for inhibiting the formation of inclusions is 0.018–0.031 wt%. The statistical trend is consistent with the report of Liu et al. [24], who indicated that the addition of a certain amount of REM (0.012–0.022 wt%) in 718H steel significantly reduced the proportion of large-sized inclusions, increased the proportion of fine inclusions, and reduced the average equivalent diameter of inclusions. However, with increasing content of REM up to 0.07 wt%, the size and number of inclusions increased significantly.

Figures 5a and b show the SEM-EDS analysis of the typical inclusions in DSS 1 alloy. The energy spectrum composition analysis demonstrates that the inclusions are mainly composed of $Al_2O_3$, MnS, and their composite inclusions. Without the addition of REM to molten steel, oxygen and sulfur elements mainly exist in the form of dissolved and deoxidized product, such as $Al_2O_3$. As REMs are added into the alloy as active elements, on the one hand, they react with oxygen and sulfur elements to form spherical or spindle-shaped $(REM)_2O_3$ and $(REM)_xS_y$. On the other hand, the inclusions of aluminosilicate, $Al_2O_3$, and sulfide in the alloy are modified into rare earth oxides, rare earth sulfides, rare earth oxide aluminum compounds, and their composite products with small sizes (Figure 5c and d). The above inclusions have greater negative free energy, which will take precedence over the formation of other oxides and sulfur oxides [18,24,34]. The micro/nanoscale REM inclusions is smaller than that of non-metallic inclusions, such as $Al_2O_3$ and MnS. Furthermore, a recent study reported the inclusions evolution pattern with the addition of different REMs in 718H steel [24]. The results showed that with the addition of REM, irregular MnS and $Al_2O_3$ inclusions were modified to elliptical REM inclusions. In addition, with the increasing content of REM, the formation process of REM inclusions was deduced as ($RE_2O_2S$, $RE_2O_3$, and $REAlO_3$) → ($RE_2O_2S$, $RE_2O_3$, and RES) → ($RE_2O_2S$ and RES). Through the inclusion of thermodynamic calculation, SEM and EDS observations are consistent with the actual precipitation sequence. However, when the content of REM increases up to 0.057 wt%, excessive REM adsorbs on the formed rare earth oxygen and sulfur inclusions, promoting the absorption of more impurity elements, such as phosphorus and sulfur, as shown in Figure 5e. In addition, excessive REM addition can increase the concentration of inclusions in the alloy, and the collision and agglomeration of inclusions are more likely to form large inclusions or dense inclusions, which is detrimental to the mechanical properties of the alloy.

## 3.3 Effect of the REM addition on mechanical properties

Figure 6a shows the effect of REM on the mechanical properties of the experimental alloys at room temperature. With the increasing content of REM, the yield strength, tensile strength, and elongation of the alloy reached the maximum value at 0.031 wt%, which are 726 ± 8 MPa, 951 ± 12 MPa, and 44 ± 2%, respectively. Compared with DSS 1 alloy, they are increased by 3.7, 4.2, and 14.1%, respectively. Figure 7 shows that the number of dimples in the fracture of DSS 1 alloy is small, and there are large inclusions at the bottom of the hole. The dimples of the middle axis in the fracture of DSS 3 alloy become more and deeper. However, the number of dimples in the DSS 4 alloy became shallow overall despite its high number. The addition of REM can modify the nonmetallic inclusions into ellipsoidal forms such as rare earth oxysulfide and rare earth sulfides, which have higher hardness and thermal expansion properties compared to $Al_2O_3$ and MnS. They can improve the coordination of deformation with the surrounding matrix [25,34–36], thereby improving the mechanical properties and fatigue life of the material [26]. In addition, the inclusion of REM can also inhibit the segregation of harmful residual elements, such as arsenic and phosphorus, at grain boundaries and enhance the grain boundary cohesion, thereby improving the grain boundary-related properties [25]. Ahn et al. [37] presented that with the addition of 0.015 wt% Gd to 27Cr–7Ni hyper DSSs, the tensile strength, hardness, and impact toughness of the alloy were improved. There are several reasons for the excellent strength and plasticity of DSS 3 alloy. First, a large number of micro/nanoscale and uniformly distributed REM inclusions were formed with the addition of REM, which makes the microstructure refined obviously as shown in Figure 1. According to the Hall–Petch equation [38,39], the yield strength increases with the refinement of grain size, which is consistent with the experimental results. With the addition of REM, there was a small amount of solution REM in the alloy, which can also play the role of solid solution strengthening, so as to improve the strength of the alloy. In addition, the fine and uniform spherical REM inclusions are usually not formed between grains along the grain boundaries, which can bond well to the matrix and are less likely to concentrate stress, thus improving the ductility of the material [17,19]. In contrast, the size and volume of inclusions in DSS 3 were reduced and evenly distributed,

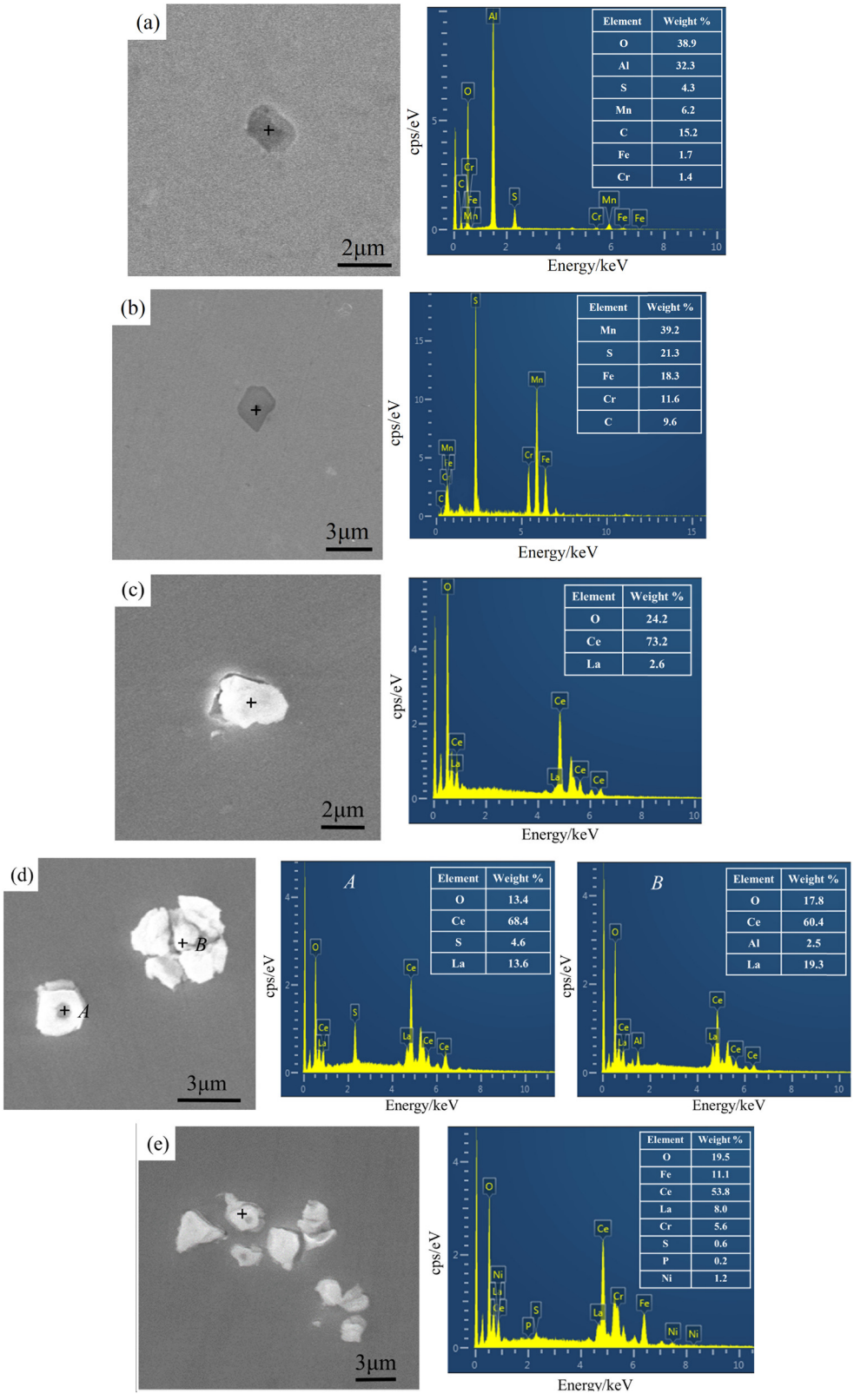


**Figure 5:** SEM-EDS analysis of inclusions in the alloys: (a and b) DSS 1, (c and d) DSS 3, and (e) DSS 4.

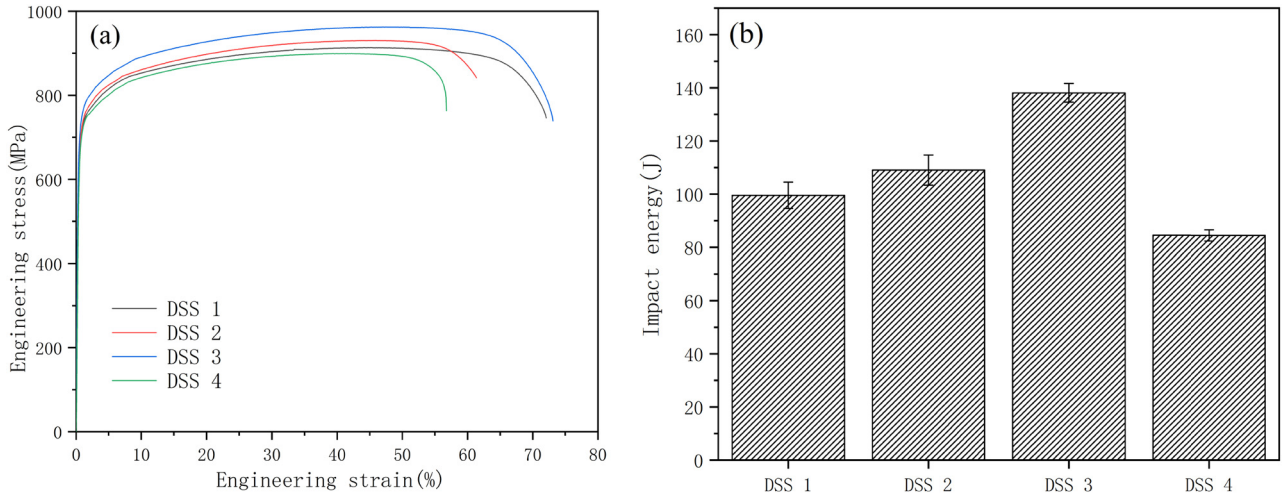


**Figure 6:** Effects of REM on the mechanical properties of the alloys: (a) tensile stress vs strain curves of solid-solution-treated specimens and (b) Charpy impact energy of solid-solution-treated specimens.

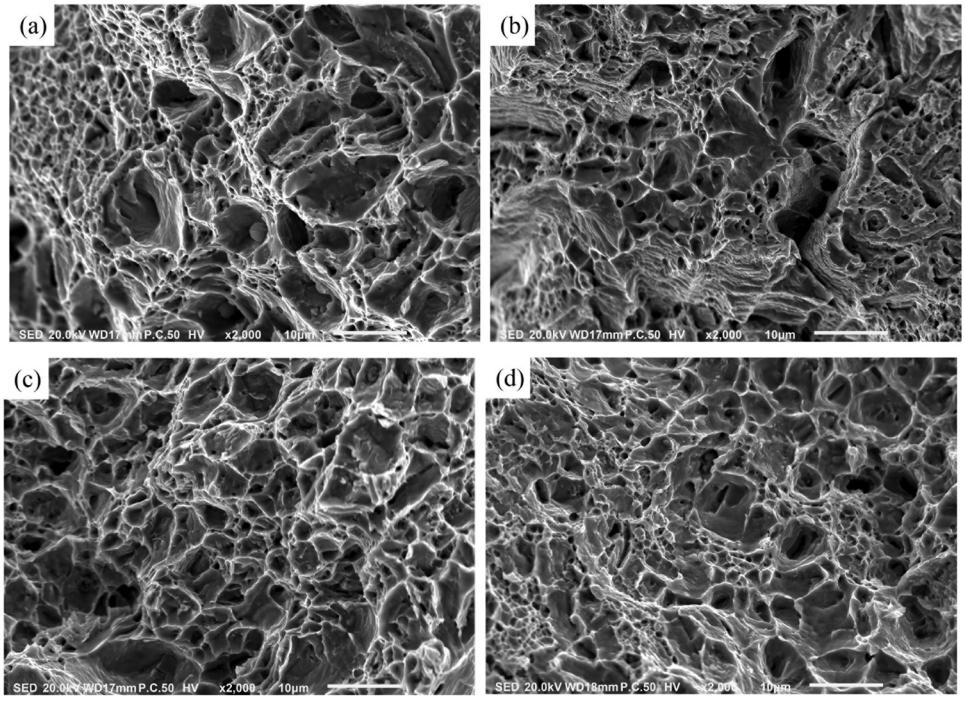


**Figure 7:** The SEM images of tensile fracture of the alloys: (a) DSS 1, (b) DSS 2, (c) DSS 3, and (d) DSS 4.

which is helpful to improve the tensile properties of the alloy. However, with the increasing content of REM (0.057 wt%), the mechanical properties of DSS 4 alloy decreased. Recent research conducted *in situ* tensile tests on 718H steel with REM content of 0.022 wt% to elucidate the mechanism of crack initiation, propagation, and inclusions shedding [24]. The results showed that when the matrix undergoes plastic deformation, cracks started to initiate and aggregate at the ends of the REM inclusions. Under continuous loading, internal cracks and boundary cracks were generated in the REM inclusions until they were finally separated from the matrix. Therefore, the larger the average diameter of REM inclusions after plastic deformation, the faster the crack propagation rate, and

thus a certain degree of strength reduction occurs. The decrease in the strength of DSS 4 alloy was most likely due to a significant increase in the average diameter and number of inclusions, which increases the crack source and crack propagation rate.

Figure 6b shows the effect of REM addition on the impact properties of the alloys at room temperature. DSS 3 has the highest impact toughness. Compared with DSS 1 alloy, the average impact toughness increases from 99.5 ± 5 to 138.1 ± 4 J. Figure 8 shows the impact fracture

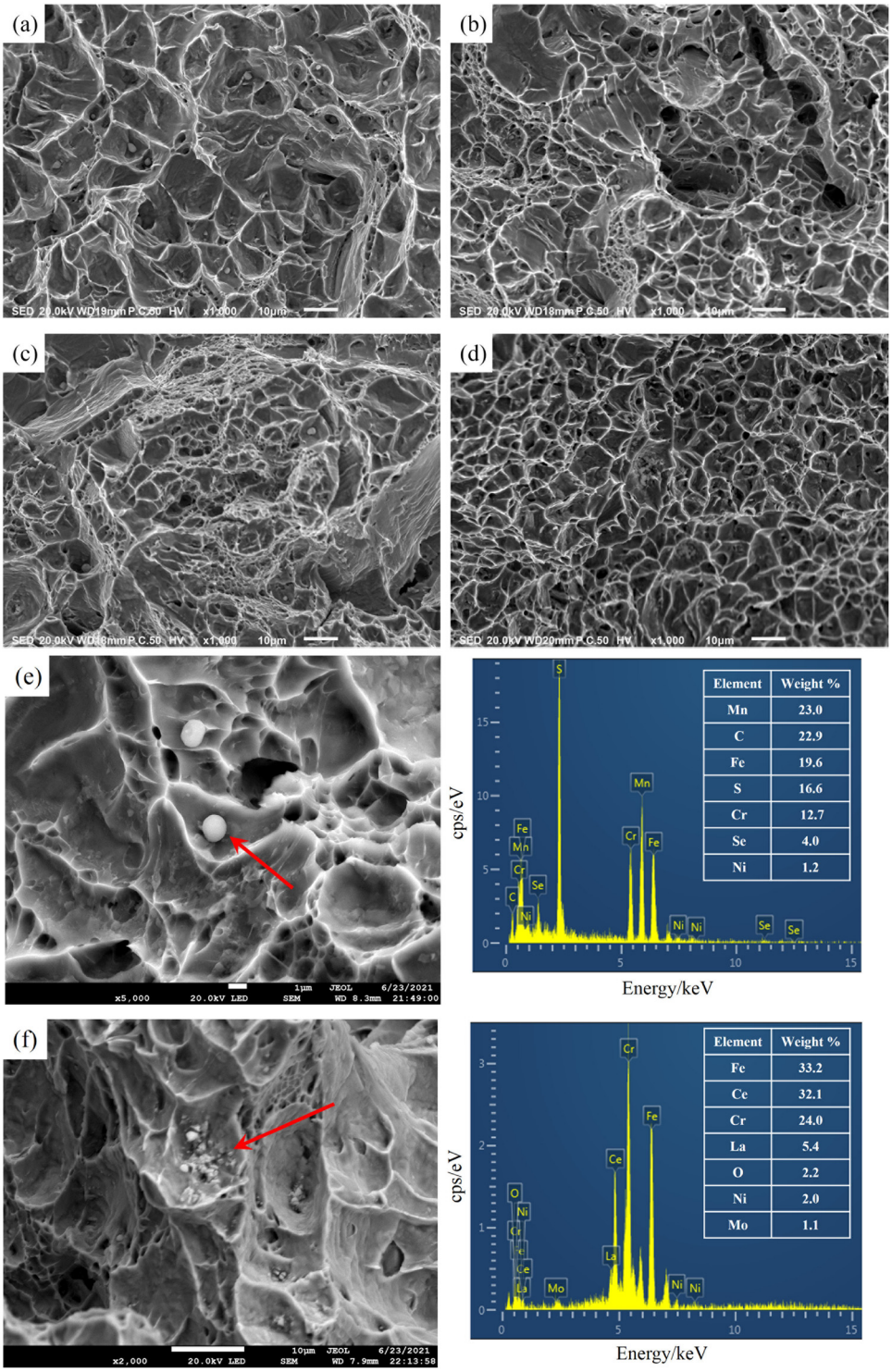


**Figure 8:** The SEM images of impact fracture of the alloys: (a) DSS 1, (b) DSS 2, (c) DSS 3, and (d) DSS 4. SEM images and its EDS peaks of (e) DSS 1 and (f) DSS 4.

and energy spectrum analysis of the samples, all of which show a ductile fracture. Figure 8a shows the fracture of DSS 1 with large and shallow dimples and large inclusion particles at the bottom of the dimples. Energy spectrum analysis (Figure 8e) shows brittle inclusions such as MnS, which are easy to become crack initiation points and reduce the toughness of the material. The number of dimples on the fracture surface of DSS 3 alloy obviously increased, and the dimples became deeper. The inclusions with large size at the bottom of the dimples decreased obviously. Although there is a large number of dimples in the fracture surface of DSS 4 alloy, there are dense aggregations of REM inclusions exist (Figure 8f). It is widely accepted that the addition of appropriate amounts of REM can purify the steel, modify irregular inclusions, and refine the grain, so as to improve the toughness of the alloy. The form of impact fracture is the interaction of crack initiation and propagation. The purification of the steel by REM addition leads to a reduction in the number of inclusions, which can significantly reduce the source of cracks. Grain refinement can effectively inhibit the expansion of cracks under impact loading and reduce grain boundary stress concentration. In addition, the micro/nanoscale ellipsoidal REM inclusions can effectively reduce the stress concentration around them. It has been reported that tiny REM inclusions have a lower activity than that of most other coarse inclusions during crack initiation and propagation [37]. The REM inclusions can produce large plastic deformation and consume more energy in the process of impact fracture, therefore improving the impact toughness. Diffusely distributed fine spherical REM inclusions can be less prone to breakage during crack extension and avoid stress concentration effectively [40]. Meanwhile, another research reported that with the increasing content of REM, REM inclusions trapped the harmful elements, such as sulfur, arsenic, and phosphorus, in high-carbon chromium-bearing steel, which gradually reduced the segregation at grain boundaries and purified the grain boundaries. The addition of REM can enhance the grain boundary strength and modify the crack extension path, and thus the transverse and longitudinal impact toughness can be improved [25]. In addition, several studies have shown that REM solute segregation at grain boundaries can increase grain boundary cohesion and improve grain boundary strength [41,42]. However, when excessive REMs were added to steel, the growth mechanism of inclusions changed from precipitation to aggregate growth [25], with a continuous increase in size and a gradual deterioration in distribution and morphology. The larger inclusions formed due to excessive REM addition have different coefficients of thermal expansion from the matrix, as shown in Figure 8f. The type of inclusion tends to cause stress concentration, which significantly increases the number of crack sources and accelerates crack expansion, leading to a sharp decrease in the impact toughness of DSS 4 alloy.

## 3.4 Effect of the REM addition on the resistance to pitting corrosion

Figure 9 shows the potentiodynamic polarization curves of the alloys in deaerated 3.5 wt% NaCl solution. The pitting potential ($E_p$) of DSS 3 alloy ($E_p$: 1.13 $V_{SCE}$) is higher than that of DSS 1 alloy ($E_p$: 1.02 $V_{SCE}$). The corrosion current density ($I_{corr}$) of DSS 3 alloy ($I_{corr}$: $9.81 \times 10^{-8}$ $A{\cdot}cm^{-2}$) is obviously lower than that of DSS 1 alloy ($I_{corr}$: $5.88 \times 10^{-7}$ $A{\cdot}cm^{-2}$). Compared with other alloys, DSS 3 alloy has a lower corrosion current density.

Figure 10 shows the SEM diagrams of the alloys after overpotential polarization test in deaerated 3.5 wt% NaCl solution. The pitting corrosion occurs in the bright area in the picture, and it can be seen that with the addition of REM, the number of pitting corrosion in the experimental alloy is less than that in DSS 1 alloy, in which DSS 3 alloy showed better results.

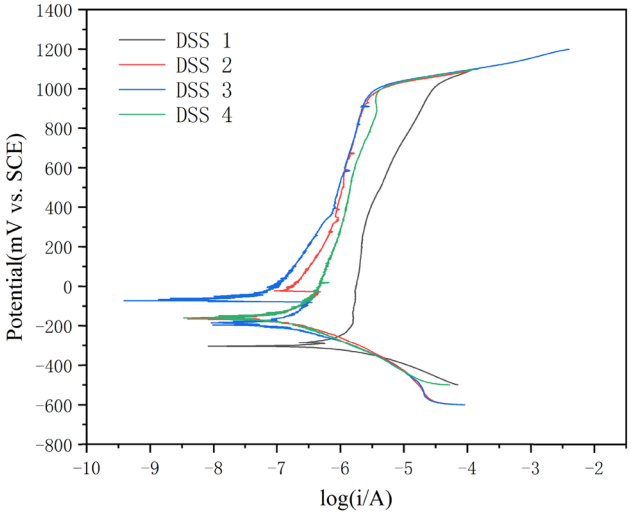


**Figure 9:** Potentiodynamic anodic polarization curves of the alloys after solution treated in deaerated 3.5 wt% NaCl solution.

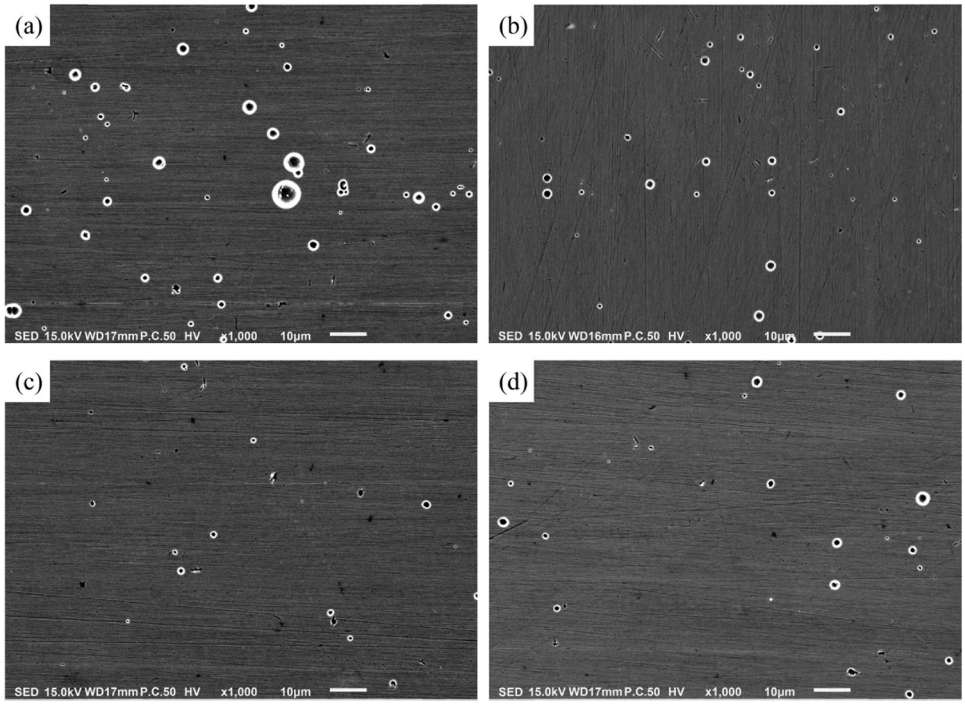


**Figure 10:** SEM images of the alloys after potentiostatic polarization test in deaerated 3.5 wt% NaCl solutions: (a) DSS 1, (b) DSS 2, (c) DSS 3, and (d) DSS 4.

## 3.5 Mechanism of the effect of REM addition on the resistance to pitting corrosion

Figure 11 shows the SEM images of the inclusions in the alloys after the overpotential anodic polarization test in deaerated 3.5 wt% NaCl solution. Non-metallic inclusions, such as $Al_2O_3$ and MnS, in DSS 1 alloy were easy to be formed at the interface between ferrite and austenite, in which the inclusions have been basically dissolved to form corrosion pits (Figure 11a). Most of the REM inclusions pitting does not happen, but very few REM inclusions cause pitting corrosion due to the gap between them and the matrix [34], which can be seen in the DSS 3 alloy (Figure 11b). However, none of the REM inclusions dissolves, and the corrosion resistance of REM inclusions seems to be higher than that of the metal matrix.

As for the cause of pitting formation, the theory of passivation film failure has been recognized by most scholars. Suter and Böhni [43] found that the region with the highest electrochemical activity is not the inclusions or metal matrix, but the interface between the inclusions and metal matrix, which is more likely to become a sensitive site for pitting corrosion. Related researches have verified that (Cr, Mn, and Al) oxidation inclusions and MnS form Cr-depleted zones with low polarization potential and strong activation [34,44]. Therefore, the areas around such inclusions are most susceptible to corrosion. Most of the non-metallic inclusions are in sharp angle shape, and the coefficient of thermal expansion is quite different from that of the metal matrix, which is easy to form cracks at the interface [34,45]. It can be directly exposed to the $Cl^-$ corrosion environment, become the origin of pitting corrosion, and then expand to the inclusions until they are dissolved. Generally, the addition of REM into an alloy can form spherical rare earth oxysulfide and rare earth oxyaluminum compounds with more negative free energy, which inhibit the formation of other coarse oxides and sulfur oxides [18,24,34]. Lu and Ives [36] have found that the thermodynamically highly stable ceria blocks the cathodic and anodic reactivity, which weakens the electrochemical corrosion of the micro-region. The small and dispersed spherical inclusions are difficult to dissolve, which can effectively prevent the corrosion of $Cl^-$ to the matrix. Since the thermal expansion coefficient of rare earth oxides is close to that of the iron matrix, it is not easy to form cracks during the hot working process [34,40]. The REM inclusions reduce the micro-gap between the matrix and the inclusions, thereby reducing the possible position of pitting corrosion. In addition, a Cr-rich area is formed around the REM inclusions, which reduces the Cr-depleted area formed around non-metallic inclusions such as ($Al_2O_3$ and

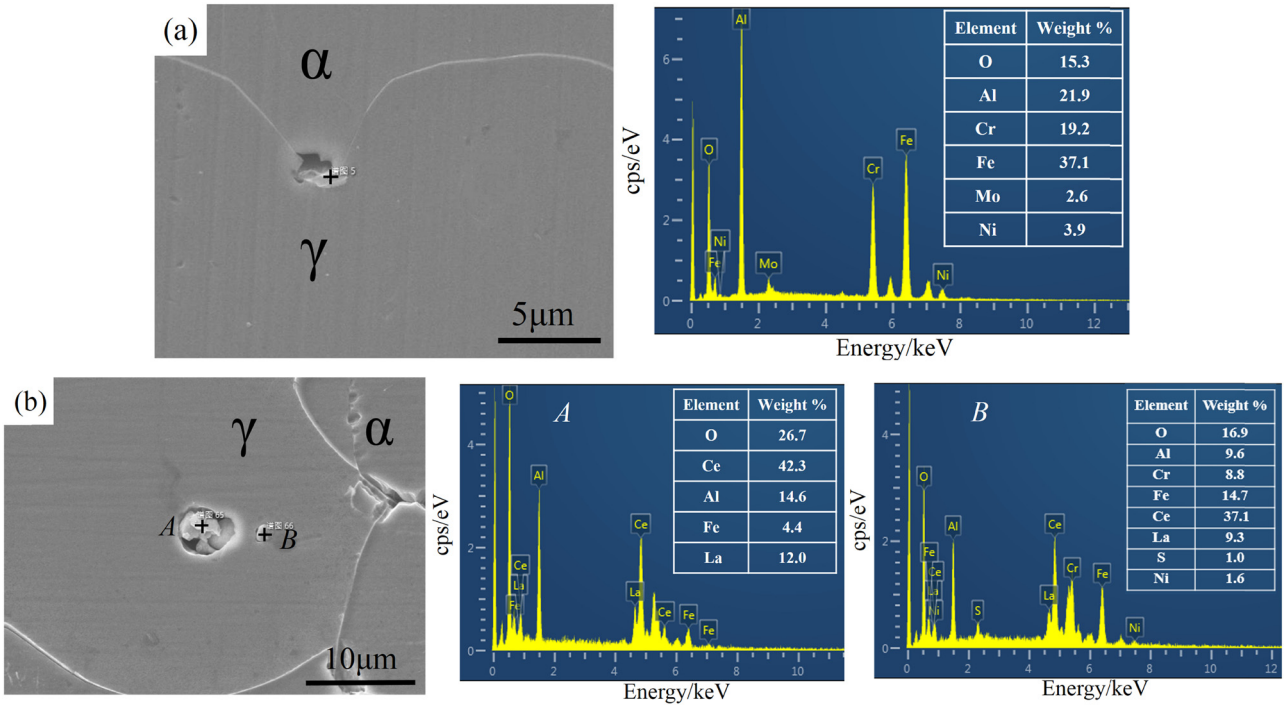


**Figure 11:** SEM-EDS analysis of inclusions in the alloys after potentiostatic polarization test in deaerated 3.5 wt% NaCl solutions: (a) DSS 1 and (b) DSS 3.

MnS) and improves the pitting corrosion resistance of the alloy [34]. Moreover, it has been discovered that the size of inclusions affects the formation of sub-stable pits, in which ultra-fine size inclusions (less than 1 μm) are difficult to form steadily growing and expanding pitting pits [46,47]. The REM inclusions marked B in Figure 11b did not form pitting pits, which is consistent with their findings. The addition of appropriate amounts of REM can purify the alloy and refine and modify the coarse and irregular inclusions. The ellipsoidal REM inclusions were likely to cause weakened electrochemical corrosion in nearby micro-regions and reduced pitting susceptibility. However, once an excessive amount of REM was added, the number of REM inclusions formed increased and the size became larger (Figures 3d and 8f), which can increase the pitting susceptibility to a certain extent and decrease the pitting resistance of the alloy.

Figure 12 shows the optical metallographic photograph of the experimental alloy after the overpotential anodic polarization test in deaerated 3.5 wt% NaCl solution. As for the DSS 1 alloy without REM addition, pitting preferentially and randomly occurs with non-metallic

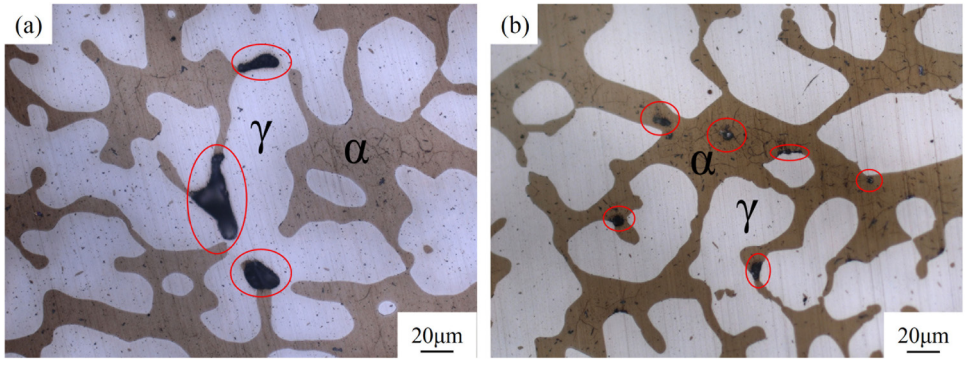


**Figure 12:** Optical microstructures of the alloys after potentiostatic polarization test in deaerated 3.5wt% NaCl solutions: (a) DSS 1 and (b) DSS 3.

inclusions in the α phase (darker color) and γ phase (lighter color) (Figure 12a). However, in DSS 3 alloys with REM, pitting occurs more randomly in the α phase and extended to the γ phase (Figure 12b). Due to the higher content of the N element in DSSs, the solubility of the N element in the γ phase is much higher than that of the α phase, which significantly increases the PREN value of the γ phase. Therefore, some scholars [48,49] have proposed to increase the N content coefficient from 16 to 30 in the DSSs calculation formula. The value of PREN for γ phase in DSS 1 ($PREN_\gamma$ = 60.3) is much higher than that of the α phase ($PREN_\alpha$ = 49.9). However, since the stable REM inclusions seem to be less susceptible to corrosion dissolution, pitting occurs more randomly in the α phase first.

# 4 Conclusion

The effects of REM on the microstructure, mechanical properties, and corrosion resistance of 27Cr–7Ni–4.5Mo–0.4N hyper DSSs were studied. The following conclusions have been drawn:

(1) The addition of REM leads to the formation of large amounts of micro/nanoscale REM inclusions, resulting in more non-spontaneously nucleated cores during solidification. With the increasing content of REM, the as-cast microstructure of the alloy is continuously refined. The same pattern occurs in the microstructure of solution treated state.
(2) The addition of REM in the range of 0.018–0.031 wt% significantly purifies the steel and reduced the number of large-size inclusions in the alloy. The average diameter and area fraction of inclusions are significantly reduced. In addition, the addition of REM contributes to modifying irregular MnS and $Al_2O_3$ to ellipsoidal REM inclusions. However, the excessive REM addition (0.057 wt%) leads to a substantial increase in the average diameter and area fraction of inclusions, with a deterioration in both distribution and morphology.
(3) The addition of appropriate amounts of REM has a significant effect on improving the strength and impact toughness of the alloy. However, excessive REM addition causes a significant increase in the number of large-size inclusions, which deteriorates the mechanical properties. The REM content should be controlled in the range of 0.018–0.031 wt% to obtain better mechanical properties.
(4) An appropriate content of REM can reduce pitting susceptibility and decrease the corrosion current density, thereby improving the pitting resistance of the alloy. The alloy with the REM content of 0.031 wt% exhibited the best resistance to pitting corrosion.

**Acknowledgments:** We appreciate the financial support of the Major Science and Technology Program of Luoyang, China (Grant No. 2101005A)

**Funding information:** The study was supported by the Major Science and Technology Program of Luoyang, China (Grant No. 2101005A).

**Author contributions:** All authors have accepted responsibility for the entire content of this manuscript and approved its submission.

**Conflict of interest:** The authors state that there is no conflict of interest.

# References

[1] Zhang, X., P. Wang, D. Z. Li, and Y. Y. Li. Multi-scale study on the heterogeneous deformation behavior in duplex stainless steel. *Journal of Materials Science & Technology*, Vol. 7213, 2021, pp. 180–188.
[2] Zhang, Y. M., C. Y. Wang, K. M. Reddy, W. Li, and X. D. Wang. Study on the deformation mechanism of a high-nitrogen duplex stainless steel with excellent mechanical properties originated from bimodal grain design. *Acta Materialia*, Vol. 226, 2022, id. 117670.
[3] Chen, W. X., C. W. Zheng, C. N. Jia, B. J. Hu, and D. Z. Li. Strain-rate dependence of the dynamic softening in a duplex stainless steel. *Materials Characterization*, Vol. 162, 2020, id. 110219.
[4] Pohl, M., O. Storz, and T. Glogowski. Studies on the degree of sensitization of hyper-duplex stainless steel 2707 at 900°C using a modified DL-EPR test. *Corrosion Science*, Vol. 185, 2021, id. 109432.
[5] Zhang, B. B., H. B. Li, S. C. Zhang, Z. H. Jiang, Y. Lin, H. Feng, et al. Effect of nitrogen on precipitation behavior of hyper duplex stainless steel S32707. *Materials Characterization*, Vol. 175, 2021, id. 111096.
[6] Kim, Y. J., S. W. Kim, H. B. Kim, C. N. Park, Y. I. Choi, and C. J. Park. Effects of the precipitation of secondary phases on the erosion-corrosion of 25% Cr duplex stainless steel. *Corrosion Science*, Vol. 152, 2019, pp. 202–210.
[7] Zhang, W. and J. Hu. Effect of annealing temperature on transformation induced plasticity effect of a lean duplex stainless steel. *Materials Characterization*, Vol. 79, 2013, pp. 37–42.
[8] Tan, H., Y. M. Jiang, B. Deng, T. Sun, J. L. Xu, and J. Li. Effect of annealing temperature on the pitting corrosion resistance of

super duplex stainless steel UNS S32750. *Materials Characterization*, Vol. 60, 2009, pp. 1049–1054.
[9] Kim, S. M., J. S. Kim, K. T. Kim, K. T. Park, and C. S. Lee. Effect of Ce addition on secondary phase transformation and mechanical properties of 27Cr-7Ni hyper duplex stainless steels. *Materials Science & Engineering, A: Structural Materials: Properties, Microstructure and Processing*, Vol. 573, 2013, pp. 27–36.
[10] Jeon, S. H., D. H. Hur, H. J. Kim, and Y. S. Park. Effect of Ce addition on the precipitation of deleterious phases and the associated intergranular corrosion resistance of 27Cr-7Ni hyper duplex stainless steels. *Corrosion Science*, Vol. 90, 2015, pp. 313–322.
[11] Świerczyńska, A., D. Fydrych, M. Landowski, G. Rogalski, and J. Łabanowski. Hydrogen embrittlement of X2CrNiMoCuN25-6-3 super duplex stainless steel welded joints under cathodic protection. *Construction and Building Materials*, Vol. 238, 2020, id. 117697.
[12] Varbai, B., T. Pickle, and K. Májlinger. Effect of heat input and role of nitrogen on the phase evolution of 2205 duplex stainless steel weldment. *International Journal of Pressure Vessels & Piping*, Vol. 176, 2019, id. 103952.
[13] Cui, Z. Y., S. S. Chen, Y. P. Dou, S. K. Han, L. W. Wang, C. Man, et al. Passivation behavior and surface chemistry of 2507 super duplex stainless steel in artificial seawater: Influence of dissolved oxygen and pH. *Corrosion Science*, Vol. 150, 2019, pp. 218–234.
[14] Scully, J. R., N. D. Budiansky, Y. Tiwary, A. S. Mikhailov, and J. L. Hudson. An alternate explanation for the abrupt current increase at the pitting potential. *Corrosion Science*, Vol. 50, 2008, pp. 316–324.
[15] Schmuki, P., H. Hildebrand, A. Friedrich, and S. Virtanen. The composition of the boundary region of MnS inclusions in stainless steel and its relevance in triggering pitting corrosion. *Corrosion Science*, Vol. 47, 2005, pp. 1239–1250.
[16] Sudesh, T. L., L. Wijesinghe, and D. J. Blackwoo. Real time pit initiation studies on stainless steels: The effect of sulphide inclusions. *Corrosion Science*, Vol. 49, 2007, pp. 1755–1764.
[17] Gupta, C. K. and N. Krishnamurthy. Extractive metallurgy of rare earths. *International Materials Reviews*, Vol. 37, 1992, pp. 197–248.
[18] Kim, S. T., S. H. Jeon, I. S. Lee, and Y. S. Park. Effects of rare earth metals addition on the resistance to pitting corrosion of super duplex stainless steel – Part 1. *Corrosion Science*, Vol. 52, 2010, pp. 1897–1904.
[19] Fruehan, R. J. The free energy of formation of $Ce_2O_2S$ and the nonstoichiometry of cerium oxides. *Metallurgical Transactions B*, Vol. 10, No. 2, 1979, pp. 143–148.
[20] NithinRaj, P., P. K. Navaneethkrishnan, K. Sekar, and M. A. Joseph. Comparative study of mechanical, corrosion and erosion-corrosion properties of cast hyper-duplex and super-duplex stainless steels. *International Journal of Minerals, Metallurgy and Materials*, Vol. 27, 2020, pp. 954–961.
[21] NithinRaj, P., S. Nithin, K. Sekar, and M. A. Joseph. Experimental investigation on dry sliding wear resistance of recently developed hyper-duplex stainless steel. *Materials Today Proceedings*, Vol. 22, 2020, pp. 2172–2178.
[22] Ma, X. C., Z. J. An, L. Chen, T. T. Mao, J. F. Wang, H. J. Long, et al. The effect of rare earth alloying on the hot workability of duplex stainless steel-A study using processing map. *Materials & Design*, Vol. 86, 2015, pp. 848–854.
[23] Ha, H. Y., C. J. Park, and H. S. Kwon. Effects of misch metal on the formation of non-metallic inclusions and the associated resistance to pitting corrosion in 25% Cr duplex stainless steels. *Scripta Materialia*, Vol. 55, 2006, pp. 991–994.
[24] Liu, H. H., P. X. Fu, H. W. Liu, Y. F. Cao, C. Sun, N. Y. Du, et al. Effects of Rare Earth elements on microstructure evolution and mechanical properties of 718H pre-hardened mold steel. *Journal of Materials Science & Technology*, Vol. 5015, 2020, pp. 245–256.
[25] Yang, C. Y., Y. K. Luan, D. Z. Li, and Y. Y. Li. Effects of rare earth elements on inclusions and impact toughness of high-carbon chromium bearing steel. *Journal of Materials Science & Technology*, Vol. 35, No. 7, 2019, pp. 1298–1308.
[26] Yang, C. Y., Y. K. Luan, D. Z. Li, Y. Y. Li, and N. U. H. Tariq. Very high cycle fatigue behavior of bearing steel with rare earth addition. *International Journal of Fatigue*, Vol. 131, 2020, id. 105263.
[27] Jiang, Z. H., P. Wang, D. Z. Li, and Y. Y. Li. Effects of rare earth on microstructure and impact toughness of low alloy Cr-Mo-V steels for hydrogenation reactor vessels. *Journal of Materials Science & Technology*, Vol. 4510, 2020, pp. 1–14.
[28] Rajasekhar, K., C. S. Harendranath, R. Raman, and S. D. Kulkarni. Microstructural evolution during solidification of austenitic stainless steel weld metals: A color metallographic and electron microprobe analysis study. *Materials Characterization*, Vol. 38, 1997, pp. 53–65.
[29] Lee, J. H., H. C. Kim, C. Y. Jo, S. K. Kim, J. H. Shim, S. Liu, et al. Microstructure evolution in directionally solidified Fe-18Cr stainless steels. *Materials Science & Engineering, A: Structural Materials: Properties, Microstructure and Processing*, Vol. 413-414, 2005, pp. 306–311.
[30] Park, Y. H. and Z. H. Lee. The effect of nitrogen and heat treatment on the microstructure and tensile properties of 25Cr-7Ni-1.5Mo-3W-xN duplex stainless steel castings. *Materials Science & Engineering, A: Structural Materials: Properties, Microstructure and Processing*, Vol. 297, 2001, pp. 78–84.
[31] Tumbull, D. and B. Vonnegut. Nucleation catalysis. *Industrial & Engineering Chemistry*, Vol. 44, 1952, pp. 1292–1298.
[32] Branfitt, B.L. Effect of carbide and nitride additions on the heterogeneous nucleation behavior of liquid iron. *Metallurgical Transactions*, Vol. 1, No. 7, 1970, pp. 1987–1995.
[33] Gao, J. Z., P. X. Fu, H. W. Liu, and D. Z. Li. Effects of rare earth on the microstructure and impact toughness of H13 steel. *Metals*, Vol. 5, 2015, pp. 383–394.
[34] Jeon, S. H., S. T. Kim, M. S. Choi, J. S. Kim, K. T. Kim, and Y. S. Park. Effects of cerium on the compositional variations in and around inclusions and the initiation and propagation of pitting corrosion in hyper duplex stainless steels. *Corrosion Science*, Vol. 75, 2013, pp. 367–375.
[35] Hashimoto, K., T. Fujimatsu, N. Tsunekage, K. Hiraoka, K. Kida, and E. C. Santos. Study of rolling contact fatigue of bearing steels in relation to various oxide inclusions. *Materials & Design*, Vol. 32, 2011, pp. 1605–1611.
[36] Lu, Y. C. and M. B. Ives. The improvement of the localized corrosion resistance of stainless steel by cerium. *Corrosion Science*, Vol. 37, 1993, pp. 1773–1784.
[37] Ahn, J. H., H. D. Junga, J. H. Im, K. H. Jung, and B. M. Moon. Influence of the addition of gadolinium on the microstructure

and mechanical properties of duplex stainless steel. *Materials Science & Engineering, A: Structural Materials: Properties, Microstructure and Processing*, Vol. 658, 2016, pp. 255–262.
[38] Hall, E.O. The deformation and ageing of mild steel: III discussion of results. *Proceedings of the Physical Society, Section B*, Vol. 64, No. 9, 1951, pp. 747–753.
[39] Petch, N. J. The cleavage strength of polycrystals. *Journal of the Iron and Steel Institute*, Vol. 174, 1953, pp. 25–28.
[40] Liu, X., J. C. Yang, L. Yang, and X. Z. Gao. Effect of Ce on inclusions and impact property of 2Cr13 stainless steel. *Journal of Iron and Steel Research, International*, Vol. 1712, 2010, pp. 59–64.
[41] Xu, Y. W. and S. H. Song. Impurity antimony-induced creep property deterioration and its suppression by rare earth cerium for a 9Cr-1Mo ferritic heat-resistant steel. *Metals*, Vol. 6, 2016, id. 187.
[42] Song, S. H., Y. W. Xu, X. M. Chen, and X. Jiang. Effect of rare earth cerium and impurity tin on the hot ductility of a Cr-Mo low alloy steel. *Journal of Rare Earths*, Vol. 34, 2016, pp. 1062–1068.
[43] Suter, T. and H. Böhni. Microelectrodes for corrosion studies in microsystems. *Electrochimica Acta*, Vol. 47, 2001, pp. 191–199.
[44] Ryan, M. P., D. E. Williams, R. J. Chater, B. M. Hutton, and D. S. Mcphail. Why stainless steel corrodes. *Nature*, Vol. 415, 2002, pp. 770–774.
[45] Szummer, A., M. Janik-Czachor, and S. Hofmann. Discontinuity of the passivating film at nonmetallic inclusions in stainless steels. *Materials Chemistry & Physics*, Vol. 34, 1993, pp. 181–183.
[46] Suter, T. and H. Böhni. Microelectrodes for studies of localized corrosion processes. *Electrochimica Acta*, Vol. 43, 1998, pp. 2843–2849.
[47] Williams, D. E., J. Stewart, and P. H. Balkwill. The nucleation, growth and stability of micropits in stainless steel. *Corrosion Science*, Vol. 36, 1994, pp. 1213–1235.
[48] Bernhardsson, S. *Proceeding, Duplex Stainless Steel'91*, Beaune Bourgogne, France, 1991, p. 185.
[49] Barteri, M., M. G. Mecozzi, and I. Nembrini. In *Duplex Stainless Steels'94*, Vol. 3, Glasgow, Scotland, 1994, p. 60.